

Encoded Prior Sliced Wasserstein AutoEncoder for Learning Latent Representations of Data

Sanjukta Krishnagopal¹[0000-0002-1556-404X] and
Jacob Bedrossian²[0000-0001-6288-0865]

¹ Gatsby Computational Neuroscience Unit, University College London, London
W1T 4JG, UK

² Department of Mathematics and Center for Scientific Computation and
Mathematical Modeling, University of Maryland College Park, Maryland 20742, USA
s.krishnagopal@ucl.ac.uk, jacob@math.umd.edu

Abstract. While variational autoencoders have been successful in several tasks, the use of conventional priors are limited in their ability to encode the underlying structure of input data. We introduce an Encoded Prior Sliced Wasserstein AutoEncoder wherein an additional prior-encoder network learns an embedding of the data manifold which preserves topological and geometric properties of the data, thus improving the structure of latent space. The autoencoder and prior-encoder networks are iteratively trained using the Sliced Wasserstein distance. The effectiveness of the learned manifold encoding is explored by traversing latent space through interpolations along *geodesics* which generate samples that lie on the data manifold and hence are more realistic compared to Euclidean interpolation. To this end, we introduce a graph-based algorithm for exploring the data manifold and interpolating along network-geodesics in latent space by maximizing the density of samples along the path while minimizing total energy. We use the 3D-spiral data to show that the prior encodes the geometry underlying the data unlike conventional autoencoders, and to demonstrate the exploration of the embedded data manifold through the network algorithm. We apply our framework to benchmarked datasets to demonstrate the advantages of learning data representations in outlier generation, latent structure, and geodesic interpolation.

Keywords: data manifold, Wasserstein autoencoder, data embedding, structure of data, latent representation, network geodesics

1 Introduction

Generative models have the potential to capture rich representations of data and use them to generate realistic outputs. In particular, Variational AutoEncoders (VAEs) [1] can capture important properties of high-dimensional data in their latent embeddings, and sample from a prior distribution to generate realistic images. While VAEs have been very successful in a variety of tasks, the use of

a simplistic standard normal prior is known to cause problems such as underfitting and over-regularization, and fails to use the network’s entire modeling capacity [2]. Most data can mathematically be thought of as living on a high dimensional manifold [3,4,5]. Gaussian or Gaussian mixture model (GMM) priors are also limited in their ability to represent geometric and topological properties of the underlying data manifold. Learning improved latent representations of this nonlinear manifold is an important problem, for which a more flexible prior may be desirable.

Conventional variational inference uses Kullback-Leibler (KL) divergence as a measure of distance between the posterior and the prior, restricting the prior distribution to cases that have tractable approximations of the KL divergence. Several works such as [6,7,8,9,10] have attempted to increase the complexity of the prior in order to obtain better latent representations. Alternately, many works such as [11,12,13,14] replace the KL divergence with an adversarial loss, however adversarial methods tend to be significantly more expensive and difficult to optimize. In higher dimensions, using a discriminator network as in adversarial approaches is a natural way of implicitly computing an equivalent of the Wasserstein-1 distance [13,15]. However, using the SW distance is much simpler and more efficient.

In this work, we introduce the Encoded Prior Sliced Wasserstein AutoEncoder (EPSWAE), which consists of a conventional autoencoder architecture and an additional prior-encoder network that learns an unconstrained prior distribution that encodes the geometry and topology of *any* data manifold. We use a type of Sliced Wasserstein (SW) distance [16] that has a closed-form for any arbitrary distribution [17]. Wasserstein distances [18] have several of the same properties as KL divergence, but often lead to better sampling [19,15], and have been used in several machine learning applications (e.g. [13,15,17]) A Sliced Wasserstein AutoEncoder (SWAE) that regularizes an autoencoder using SW distance was proposed in [20]. Several works improve the SW distance through additional optimizations [21,22], and show improved generation, however involve additional training and use a fixed (usually Gaussian) prior. Here we use a nonlinear version of the SW distance to improve latent representations. Additionally, we introduce a structural consistency term based on penalties used in [14], that encourages the latent space to be isometric to the feature space and improves latent representation.

A key contribution of our work is the graph-based geodesic-interpolation algorithm. Conventionally, VAEs use Euclidean interpolation between two points in latent space. However, since data manifolds typically have curvature, this is an unintuitive distance metric that can lead to unrealistic intermediate points. Our goal is to learn a true representation of the underlying data manifold, hence it is natural to interpolate along the manifold geodesics in latent space. Several works such as [23,24] endow the latent space with a Riemannian geometry and measure corresponding distances, however these are difficult and involve explicitly solving expensive ordinary differential equations.

There exists limited work on integrating graphical structures with generative models [25], and many such approaches aren't robust to noise [26]. In this work, we introduce 'network-geodesics', a graph-based method for interpolating along a manifold in latent space, that maximizes sample density along paths while minimizing total energy. This involves first generating a distance graph between samples from the prior. Then this network is non-uniformly thresholded such that the set of allowable paths from a given sample traverse high density regions through short hops. Lastly, we use a shortest path algorithm like Dijkstra's algorithm [27] to identify the lowest 'energy' path between two samples through the allowable paths. Since the prior is trained to learn the data manifold, the resulting network-geodesic curves give a notion of distance on the manifold and can be used to generate realistic interpolation points with relatively few prior samples.

The novel contributions of this work are:

- We introduce a novel architecture, EPSWAE, that consists of an additional prior-encoder network that is efficiently and independently trained (without expensive adversarial methods) in order to learn a prior that encodes the geometric and topological properties of the input data.
- We introduce a novel graph-based method for interpolating along network-geodesics in latent space through maximizing sample density while minimizing total energy. We show that it generates natural interpolations through realistic images.

2 EPSWAE

In the following sections, we provide a detailed description of the methods used in training the additional prior-encoder network to learn latent manifolds, and approximating network geodesics on these manifolds.

2.1 Sliced Wasserstein Distance

Wasserstein distances are a natural metric for measuring distances between probability distributions, however they are difficult to compute in dimensions two and higher. The Sliced Wasserstein distance d_{SW} averages over the Wasserstein distance of 1D projections (see Appendix A for derivation). Several works (e.g. [28,21]) discuss why a conventional SW distance may be sub-optimal as a large number of linear projections may be required to distinguish two distributions. In this work we use a Nonlinear Sliced Wasserstein distance (d_{NSW}), an averaging procedure over (random) *nonlinear* 1D projections, between two distributions μ and ν defined as:

$$d_{NSW}(\mu, \nu) = \mathbb{E}d_{SW}(\mathcal{N}_*^{\zeta, \gamma} \mu, \mathcal{N}_*^{\zeta, \gamma} \nu) \approx \frac{1}{L} \sum_{\ell=1}^L d_{SW}(\mathcal{N}_*^{\zeta_\ell, \gamma_\ell} \mu, \mathcal{N}_*^{\zeta_\ell, \gamma_\ell} \nu) \quad (1)$$

where L is the number of nonlinear transformations, and ζ, γ are chosen to be normal random variables with mean 0, and variance matching that of μ , and \mathcal{N} is defined below. We define the “push-forward” (also known as “random variable transform”) as follows: given any function $f : X \rightarrow Z$ and probability measure μ , we define $f_*\mu(A) = \mu(f^{-1}(A))$ for all $A \subset Z$ measurable. Most importantly, to generate samples of $z \sim f_*\mu$ one simply generates $x \sim \mu$ and defines $z = f(x)$. The nonlinear transformations are related to a special case of the generalized SW distance [28] and are motivated by simplicity, tail-behavior considerations (such as boundedness and non-saturation of nonlinearity), along with computational efficiency. Other choices of nonlinearity that may be more appropriate for specific data can easily be incorporated into our method.

2.2 Algorithm Details

In the Encoded Prior Sliced Wasserstein AutoEncoder (EPSWAE) (see Fig. 1 for schematic), let’s define the data encoder as Ψ_E , the decoder Ψ_D , and the prior-encoder as Ψ_{PE} , each with parameters $\phi_E, \phi_D, \phi_{PE}$ respectively. Input samples $\mathbf{x}^{(j)} \sim P_X$, where P_X is the probability distribution of the input data, are passed through Ψ_E to generate posterior samples $\mathbf{z}^{(j)} \sim (\Psi_E)_*P_X$ by setting $\mathbf{z}^{(j)} = \Psi_E(\mathbf{x}^{(j)})$. Similarly, prior-encoder input samples $\xi^{(j)} \sim \mu$, where μ is the probability distribution of the input to the prior-encoder (chosen to be a mixture of Gaussians) from a distribution, are passed through Ψ_{PE} to generate prior samples $\mathbf{y}^{(j)} \sim (\Psi_{PE})_*\mu$ by setting $\mathbf{y}^{(j)} = \Psi_{PE}(\xi^{(j)})$. The prior-encoder network and the autoencoder (data encoder and decoder) network are trained *iteratively* in a two step process:

1. Given a minibatch, parameters of the autoencoder (ϕ_E, ϕ_D) are trained for k_1 steps while parameters of the prior encoder (ϕ_{PE}) are fixed. The loss function for the autoencoder consists of the reconstruction error, the NSW distance, and a Feature Structural Consistency (FSC) term \mathcal{L}_{FSC} :

$$\mathcal{L}_{AE} = \alpha \mathbb{E}_{\mathbf{x} \sim P_X} \mathcal{L}_{rec}(\mathbf{x}, \bar{\mathbf{x}}) + \beta d_{NSW}((\Psi_E)_*P_X, (\Psi_{PE})_*\mu) + \kappa \mathcal{L}_{FSC}, \quad (2)$$

where $\bar{\mathbf{x}} = \Psi_D(\Psi_E(\mathbf{x}))$ is the autoencoder output. Note that d_{NSW} is efficiently computed just from samples of the distributions.

In this measure theoretic notation, $(\Psi_E)_*P_X$ is the posterior distribution (denoted as $q_{\phi_E}(z|x)$ in Bayesian literature), and $(\Psi_{PE})_*\mu$ is the prior distribution (denoted as $p_{\phi_{PE}}(z)$ in Bayesian literature). Similar to β -VAE ([29]), the hyperparameters α, β, κ are tuneable.

\mathcal{L}_{FSC} (adapted from [14]) encourages relative distances in feature space to be preserved in latent space, where features are extracted at the output of the last convolutional layer in the encoder (or at input data if no convolutional layers are present).

2. In the second step of minimization, the parameters of the prior-encoder (Ψ_{PE}) are trained for k_2 steps while parameters of the autoencoder (ϕ_E, ϕ_D) are fixed. The loss function for the prior-encoder consists of the NSW distance between the prior and posterior:

$$\mathcal{L}_{PE}(\mathbf{x}) = d_{NSW}((\Psi_E)_*P_X, (\Psi_{PE})_*\mu). \quad (3)$$

The pseudocode is outlined in Appendix B. Additional architecture and training details for the experiments in this paper are in Appendix C.

2.3 Interpolation and approximate geodesics

EPSWAE attempts to learn a representation of the embedded manifold geometry that the data lies along. The question arises: how does one make use of this representation? A natural way of interpolating data which lies on a manifold is through geodesics or paths on the manifold which traverse dense regions. Here we present a network algorithm for efficiently approximating network-geodesics with relatively few, noisy samples from the prior, by encouraging connections through high density regions of latent space while minimizing total energy, where energy is analogous to potential energy in a spring network.

1. Gather samples of the posterior $(\Psi_E)_*P_X$, i.e., $\Psi_E(x)$ with x is a minibatch of data. Additional prior samples can be used to supplement this if desired;
2. For each sample j , compute the *average* Euclidean distance c_j of the k -nearest neighbors;
3. Generate a thresholded network: Let samples be represented as nodes. For a given threshold value t , sample j is connected to sample i with edge weight $d^h(i, j)$ if $d(i, j) < t \cdot c_j$. Here h is the energy parameter in the edge weight (chosen to be 1 or 2 in experiments, with $h = 2$ encouraging shorter hops). Sample-specific thresholding, i.e., thresholding dependent on c_j , increases the probability of a ‘central’ node having a connection. Thus, this encourages (1) paths through high density regions, i.e., high-degree nodes, and (2) traversal of latent space through short hops as a consequence of localization of paths, i.e., paths existing only between nearby points due to thresholding.
4. Continue increasing t until the graph is connected, i.e., there exists a path, direct or indirect, from every sample to every other sample. Then, use Dijkstra’s algorithm [27] to identify network-geodesics with least total energy through allowable paths on the thresholded network.

3 Experiments

We run experiments using EPSWAE on three datasets. First, we use a 3D spiral data, where the latent space can be visualized easily, to demonstrate that the learned prior captures the geometry of the 3D spiral. We also present here the advantages of the network-geodesic interpolation over linear interpolation. Then we present interpolation and generation results on the MNIST [30] and CelebA [31] datasets.

3.1 Architecture

The schematic of the architecture is presented in Fig. 1(a). Note that the specifics of the layers shown in this schematic are for the image datasets MNIST and

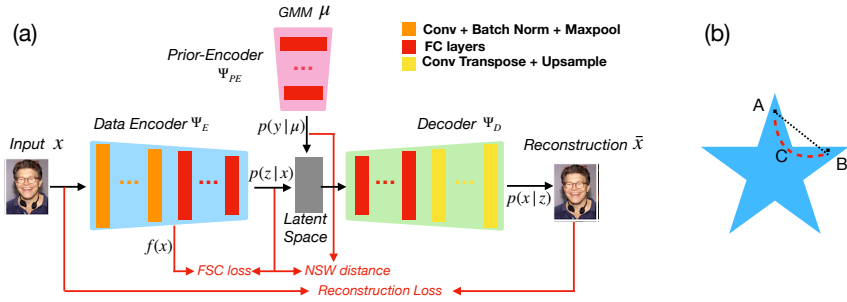


Fig. 1. (a) is a schematic of the EPSWAE architecture. The red arrows indicate calculation of the loss terms. The prior-encoder generates a prior in latent space. (b) is simple example of a shape where interpolating between points A and B ‘through the manifold’ (red dashed line through point C) is desired, since linear interpolation (black line) leads out of the concave hull.

CelebA, the 3D Spiral data does not have convolutional layers. Details of the architecture, training, and hyperparameters for each dataset are given in Appendix C. The optimizer Adam [32] with a learning rate of 0.001 was used for learning in both networks: the prior-encoder and the autoencoder.

3.2 Learning a latent manifold

We consider a 3D spiral randomly embedded to 40D space with the input of Gaussian noise. For these tests, the data encoder, prior-encoder, and decoder all consist of three Fully Connected (FC) layers with 40 nodes each and ReLU activations.

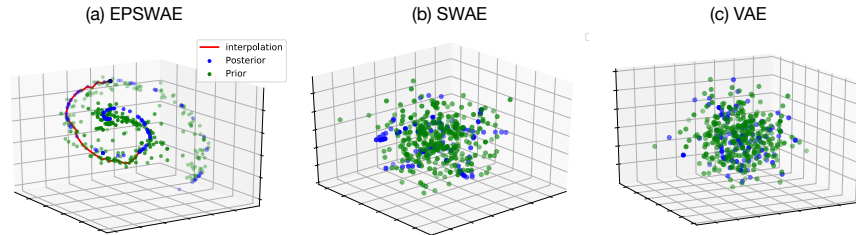


Fig. 2. Comparison of EPSWAE with baselines SWAE [20] and VAE [1]. All figures are generated after 100 epochs with a lr=0.01, and batch size =100. For EPSWAE, $k_1 = 1, k_2 = 2, \alpha = 1, \beta = 0.1, \kappa = 0.001$.

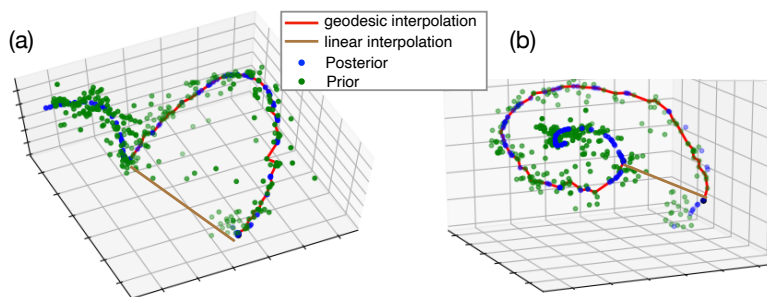


Fig. 3. (a) side view and (b) top view of samples of the prior (green) and posterior (blue) in 3D latent space generated by EPSWAE after 100 epochs on the high dimensional input. The red line shows the interpolation along network-geodesics between two prior samples. The brown line shows the trajectory of linear interpolation between two points on the spiral.

Figure 2 compares the shape of the prior in our EPSWAE model with conventional baselines SWAE [20] (without a prior encoder) and VAE [1]. In the absence of the prior encoder network that is trained specifically to learn the data manifold, SWAE and VAE fail in learning the geometry of the spiral. On the other hand, EPSWAE is seen to significantly outperform them in learning an improved latent representation. The VAE uses KL divergence in the loss, which constrains the prior to be sampled from a Gaussian distribution. While the vanilla SWAE uses the SW distance, the prior remains a Gaussian, leading to an unnatural embedding of the data manifold.

As seen in Figure 3, after training, the posterior matches the spiral almost exactly and the prior learns the geometry of the spiral. A Nonlinear Sliced Wasserstein (NSW) distance and structural consistency term (where latent space is isometric with data space since convolutional layers aren't used) are used in the loss in Eqns. 2 and 3. A comparison highlighting the effects of these terms is shown in Fig. 6 in the Appendix D.

Manifold interpolation (in red in Fig. 3) uses the network-algorithm outlined in Section 2.3. The interpolation is seen to have the desired form on the manifold, i.e., it approximates geodesics on the manifold. The larger the number of samples of the prior, the smoother the corresponding interpolation. In contrast, linear interpolation (brown line) between two points on the spiral does not capture the geometry at all, and goes through regions that are largely empty and untrained. In higher dimensional datasets, this may result in unrealistic interpolation.

3.3 Generation and outliers in latent space

In order to demonstrate one of the advantages of using a learning an improved latent structure that encodes the structure of the data itself, we consider generation with an increased probability of sampling from outliers off the manifold,

i.e., by increasing the standard deviation of the distribution that feeds into the prior encoder. Studying generation from outliers is informative in the study of how data is encoded in the latent space. In Fig. 4 compare our results with the baseline SWAE [20] in order to assess the effect of the prior encoder in improving latent structure. It is worth noting that while there exist several recent works that build upon SWAE for better generation, they do not attempt to solve the same problem as ours (learning latent manifolds). As seen in Fig. 4, the behavior of SWAE and EPSWAE at outliers is very different. For large σ , SWAE tends to generate unrealistic faces with distorted colorations, whereas EPSWAE is more likely to generate realistic faces (albiet with increased mode collapse at large σ). We see that EPSWAE encodes coherent information in a large region of latent space as a consequence of nonlinear transformations through the prior encoder. Since we are not competing with state of the art in generation here, we use downsized images and a small, unsophisticated model compared to state of the art methods. Both SWAE and EPSWAE use the same data encoder and decoder, and are independently optimized: the encoder is (after downsizing CelebA images to 64×64) Conv (3,16,3) \rightarrow BatchNorm \rightarrow ReLu \rightarrow MaxPool (2,2) \rightarrow Conv (16,32,3) \rightarrow BatchNorm \rightarrow ReLu \rightarrow MaxPool (2,2) \rightarrow Conv (32,64,3) \rightarrow BatchNorm \rightarrow ReLu followed by two FC layers of 512 and 256 nodes respectively with a leaky ReLu nonlinearity outputting a 128D latent representation and the decoder is the reverse (replace Conv layers with Conv-transpose and MaxPool with Upsample). See Appendix C for more details and hyperparameter values.



Fig. 4. Images generated after 100 epochs from prior samples in (a) EPSWAE (b) Baseline SWAE at increasing standard deviations σ , i.e., progressively more ‘outlying’.

We also present a comparison with SWAE on CelebA generation from samples around the mean in Appendix H, and find that EPSWAE sees a marginal improvement in the quality of faces. Comparison on MNIST is shown in Appendix G, EPSWAE generation is more natural, whereas both other baselines generate some bloated and unidentifiable numbers.

3.4 Interpolation

In this paper, we introduce a graph-based algorithm that interpolates over network-geodesics in curved latent manifolds, thus capturing properties of the structure of the data manifold. Here we show that we obtain smooth interpolation using the network-geodesics algorithm, in contrast with linear interpolations that often tend to generate unrealistic intermediate images.

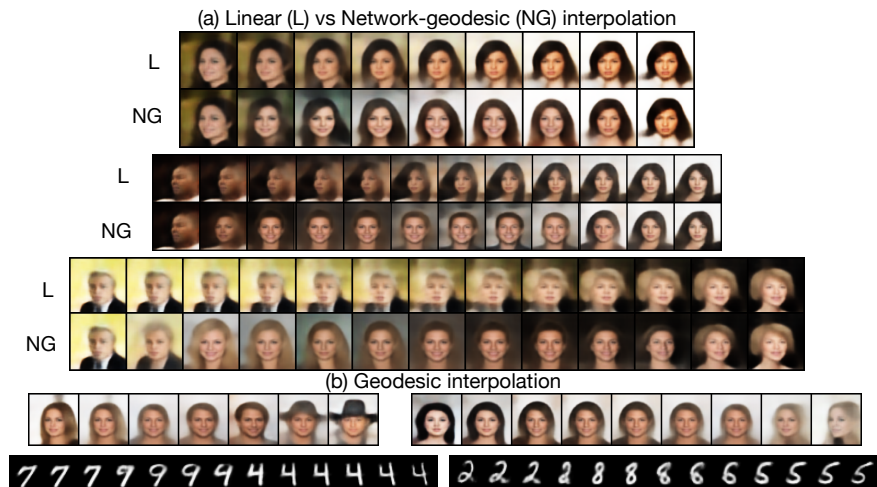


Fig. 5. (a) Comparison of linear vs geodesic interpolation using EPSWAE. The top row of each row-pair is linear, and the bottom is geodesic-interpolation. (b) Randomly chosen instances for geodesic interpolations for MNIST and CelebA. The first and last images are reconstructions of real data, and the interpolations traverse through samples of the prior using the network-geodesic algorithm. A total of 400 samples are used in all cases.

The start and end points are the same for equivalent comparisons and correspond to real images (posterior samples). Figure 5(a) presents a comparison of linear interpolation (top) vs interpolation through network-geodesics (bottom) described in Section 2.3 on CelebA. One can see that linear interpolations often go through unrealistic images (this corresponds to regions in latent space where training is limited), whereas geodesic interpolations go through more realistic

and less blurry faces. This also serves as evidence, that the latent space for CelebA contains some natural structure that can be exploited.

Figure 5 (b) shows examples of interpolations on MNIST and CelebA datasets. MNIST interpolations are smooth and intuitive, for instance, in the bottom left MNIST panel in Fig. 5(b), the top part of a ‘7’ first changes to a ‘9’ naturally, followed by transformation of the ‘9’ to a ‘4’. Interpolation along network-geodesics ensures that reconstructions of intermediate samples are realistic. Interpolations on CelebA are smooth and pass through intermediate images that could arguably pass for celebrities these days. The state of the art interpolations along network-geodesics on the manifold indicate that the learned prior does indeed encode the data manifold. For all interpolations shown in Fig. 5, we use energy parameter $h = 2$. Comparisons between interpolations corresponding to $h = 1$ and $h = 2$ are presented in Appendix 10. In experiments, energy parameter is not found to have a significant impact on the quality of interpolations. Additionally, comparisons of linear interpolation between equivalent networks of EPSWAE and SWAE are presented in Appendix J which shows that EPSWAE interpolations outperform equivalent SWAE interpolation.

4 Conclusion

We introduce the Encoded Prior Sliced Wasserstein AutoEncoder (EPSWAE) that learns improved latent representations through training an encoded prior to approximate an embedding of the data manifold that preserves geometric and topological properties. The learning of an arbitrary shaped prior is facilitated by the use of the Sliced Wasserstein distance, which can be efficiently computed from samples only. We use a nonlinear variant of SW distance to capture differences between two distributions more efficiently, and employ a feature structural consistency term to improve the latent space representation. Finally, we introduce an energy-based algorithm to identify network-geodesics in latent space that maximize path density while minimizing total energy. We demonstrate EPSWAE’s ability to learn the geometry and topology of a 3D spiral from a noisy 40D embedding. We also show that our model embeds information in large regions of latent space, leading to better outlier generation. Lastly, we show that our geodesic interpolation results on MNIST and CelebA are efficient and comparable to state of the art techniques. Our code is publicly available at github.com/chimeraki/EPSWAE.

References

1. D. P. Kingma and M. Welling. Auto-encoding variational bayes. In *International Conference on Learning Representations.*, 2014.
2. Yuri Burda, Roger B. Grosse, and R. Salakhutdinov. Importance weighted autoencoders. *CoRR*, abs/1509.00519, 2016.
3. Haw-Minn Lu, Yeshaiah Fainman, and Robert Hecht-Nielsen. Image manifolds. In *Applications of Artificial Neural Networks in Image Processing III*, volume 3307, pages 52–63. International Society for Optics and Photonics, 1998.
4. Kilian Q Weinberger and Lawrence K Saul. Unsupervised learning of image manifolds by semidefinite programming. *International journal of computer vision*, 70(1):77–90, 2006.
5. Charles Fefferman, Sanjoy Mitter, and Hariharan Narayanan. Testing the manifold hypothesis. *Journal of the American Mathematical Society*, 29(4):983–1049, 2016.
6. Nat Dilokthanakul, Pedro AM Mediano, Marta Garnelo, Matthew CH Lee, Hugh Salimbeni, Kai Arulkumaran, and Murray Shanahan. Deep unsupervised clustering with gaussian mixture variational autoencoders. *arXiv preprint arXiv:1611.02648*, 2016.
7. Hiroshi Takahashi, Tomoharu Iwata, Yuki Yamanaka, Masanori Yamada, and Satoshi Yagi. Variational autoencoder with implicit optimal priors. In *Proceedings of the AAAI Conference on Artificial Intelligence*, volume 33, pages 5066–5073, 2019.
8. Chunsheng Guo, Jialuo Zhou, Huahua Chen, Na Ying, Jianwu Zhang, and Di Zhou. Variational autoencoder with optimizing gaussian mixture model priors. *IEEE Access*, 8:43992–44005, 2020.
9. Prasoon Goyal, Zhiting Hu, Xiaodan Liang, Chenyu Wang, and Eric P Xing. Nonparametric variational auto-encoders for hierarchical representation learning. In *Proceedings of the IEEE International Conference on Computer Vision*, pages 5094–5102, 2017.
10. Jakub Tomczak and Max Welling. Vae with a vampprior. In *International Conference on Artificial Intelligence and Statistics*, pages 1214–1223, 2018.
11. Hui-Po Wang, Wen-Hsiao Peng, and Wei-Jan Ko. Learning priors for adversarial autoencoders. *APSIPA Transactions on Signal and Information Processing*, 9, 2020.
12. Alireza Makhzani, Jonathon Shlens, Navdeep Jaitly, Ian Goodfellow, and Brendan Frey. Adversarial autoencoders. *arXiv preprint arXiv:1511.05644*, 2015.
13. Martin Arjovsky, Soumith Chintala, and Léon Bottou. Wasserstein GAN. *arXiv preprint arXiv:1701.07875*, 2017.
14. Tim Sainburg, Marvin Thielk, Brad Theilman, Benjamin Migliori, and Timothy Gentner. Generative adversarial interpolative autoencoding: adversarial training on latent space interpolations encourage convex latent distributions. *arXiv preprint arXiv:1807.06650*, 2018.
15. I. Tolstikhin, O. Bousquet, S. Gelly, and B. Schölkopf. Wasserstein auto-encoders. *ArXiv*, abs/1711.01558, 2018.
16. Nicolas Bonneel, Julien Rabin, Gabriel Peyré, and Hanspeter Pfister. Sliced and radon wasserstein barycenters of measures. *Journal of Mathematical Imaging and Vision*, 51(1):22–45, 2015.
17. Soheil Kolouri, Gustavo K Rohde, and Heiko Hoffmann. Sliced wasserstein distance for learning gaussian mixture models. In *Proceedings of the IEEE Conference on Computer Vision and Pattern Recognition*, pages 3427–3436, 2018.

18. Cédric Villani. *Topics in optimal transportation*. Number 58. American Mathematical Soc., 2003.
19. Ishaan Gulrajani, Faruk Ahmed, Martin Arjovsky, Vincent Dumoulin, and Aaron C Courville. Improved training of wasserstein gans. In *Advances in neural information processing systems*, pages 5767–5777, 2017.
20. Soheil Kolouri, Phillip E Pope, Charles E Martin, and Gustavo K Rohde. Sliced wasserstein auto-encoders. In *International Conference on Learning Representations*, 2018.
21. Ishan Deshpande, Yuan-Ting Hu, Ruoyu Sun, Ayis Pyrros, Nasir Siddiqui, Sanmi Koyejo, Zhizhen Zhao, David Forsyth, and Alexander G Schwing. Max-sliced Wasserstein distance and its use for GANs. In *Proceedings of the IEEE conference on computer vision and pattern recognition*, pages 10648–10656, 2019.
22. Xiongjie Chen, Yongxin Yang, and Yunpeng Li. Augmented sliced wasserstein distances. *arXiv preprint arXiv:2006.08812*, 2020.
23. Hang Shao, Abhishek Kumar, and P Thomas Fletcher. The riemannian geometry of deep generative models. In *Proceedings of the IEEE Conference on Computer Vision and Pattern Recognition Workshops*, pages 315–323, 2018.
24. Nina Miolane and Susan Holmes. Learning weighted submanifolds with variational autoencoders and riemannian variational autoencoders. In *Proceedings of the IEEE/CVF Conference on Computer Vision and Pattern Recognition*, pages 14503–14511, 2020.
25. Thomas N Kipf and Max Welling. Variational graph auto-encoders. *NIPS Workshop on Bayesian Deep Learning*, 2016.
26. Barak Sober, Ingrid Daubechies, and Robert Ravier. Approximating the riemannian metric from point clouds via manifold moving least squares. *arXiv preprint arXiv:2007.09885*, 2020.
27. Edsger W Dijkstra. A note on two problems in connexion with graphs. *Numerische mathematik*, 1(1):269–271, 1959.
28. Soheil Kolouri, Kimia Nadjahi, Umut Simsekli, Roland Badeau, and Gustavo Rohde. Generalized sliced wasserstein distances. In *Advances in Neural Information Processing Systems*, pages 261–272, 2019.
29. Irina Higgins, Loic Matthey, Arka Pal, Christopher Burgess, Xavier Glorot, Matthew Botvinick, Shakir Mohamed, and Alexander Lerchner. beta-VAE: Learning basic visual concepts with a constrained variational framework. 2016.
30. Yann LeCun, Corinna Cortes, and CJ Burges. Mnist handwritten digit database. *ATT Labs [Online]*. Available: <http://yann.lecun.com/exdb/mnist>, 2, 2010.
31. Ziwei Liu, Ping Luo, Xiaogang Wang, and Xiaoou Tang. Large-scale celebfaces attributes (celeba) dataset. *Retrieved August*, 15:2018, 2018.
32. Diederik Kingma and Jimmy Ba. Adam: A method for stochastic optimization. *International Conference on Learning Representations*, 12 2014.
33. Nicolas Bonnotte. *Unidimensional and evolution methods for optimal transportation*. PhD thesis, Paris 11, 2013.
34. Chen-Yu Lee, Tanmay Batra, Mohammad Haris Baig, and Daniel Ulbricht. Sliced wasserstein discrepancy for unsupervised domain adaptation. In *Proceedings of the IEEE Conference on Computer Vision and Pattern Recognition*, pages 10285–10295, 2019.
35. Khai Nguyen, Nhat Ho, Tung Pham, and Hung Bui. Distributional sliced-wasserstein and applications to generative modeling. *arXiv preprint arXiv:2002.07367*, 2020.

A Background on the sliced Wasserstein distance

Wasserstein distances provide a natural metric for measuring distances between probability distributions based on optimal transport, i.e., the cost of deforming one probability distribution into another. For a measurable cost function $c(x, y)$ for $x, y \in \mathbb{R}^d$, and probability distributions μ and ν on \mathbb{R}^d , we define the p -Wasserstein distance between the distributions as

$$d_{W,p}(\mu, \nu) = \inf_{\Gamma \in \Pi(\mu, \nu)} \left(\int_{\mathbb{R}^d \times \mathbb{R}^d} c^p(x, y) d\Gamma(x, y) \right)^{1/p}, \quad (4)$$

where Π is the set of all joint distributions with marginals μ and ν (see [18]).

This Wasserstein distance between probability distributions is extremely difficult and computationally intensive in dimensions two and higher, i.e., $d \geq 2$. However, in dimension one, there exists a closed-form solution [18]. A simple algorithm for computing the 1D Wasserstein distance is given as follows (see for example [20]): (a) Generate N one dimensional i.i.d samples $x_j \sim \mu, y_j \sim \nu$; (b) sort each list $X = [x_1, \dots, x_N], Y = [y_1, \dots, y_N]$ into ascending order denoted by \tilde{X}, \tilde{Y} respectively; (c) define the approximation to the 1D p -Wasserstein distance

$$d_{W,p}(\mu, \nu) \approx \left(\frac{1}{N} \sum_{j=1}^N c^p(\tilde{x}_j, \tilde{y}_j) \right)^{1/p}, \quad (5)$$

where $\tilde{x}_j \in \tilde{X}, \tilde{y}_j \in \tilde{Y}$. The Sliced Wasserstein (SW) distance defines a metric on probability measures [33] which provides an alternative to Eqn. 4 by exploiting the computational feasibility of the 1D Wasserstein distance in Eqn. 5. It involves averaging over one-dimensional orthogonal projections $\pi^\theta x := (\theta \cdot x)\theta$ as follows:

$$d_{SW}(\mu, \nu) = \left(\int_{\mathbb{S}^{d-1}} d_{W,p}^p(\pi_*^\theta \mu, \pi_*^\theta \nu) dS(\theta) \right)^{1/p}, \quad (6)$$

The SW distance has seen a variety of implementations [16,17,34].

The integral in Eqn. 6 can be easily approximated by sampling M random one-dimensional vectors θ_k uniformly on \mathbb{S}^{d-1} and computing

$$d_{SW}(\mu, \nu) \approx \left(\frac{1}{M} \sum_{k=1}^M d_{W,p}^p(\pi_*^{\theta_k} \mu, \pi_*^{\theta_k} \nu) \right)^{1/p}. \quad (7)$$

Several works (for example [35,21]) have discussed reasons why this often does not result in the best computational method. Linear projections may be sub-optimal for extracting information about the differences between μ and ν , since a large number of linear projections may be required to get an accurate approximation for d_{SW} . Several works have suggested possible methods for improving the effectiveness of the SW distance [22,28,35,21]. In contrast, we use a Nonlinear Sliced Wasserstein (NSW) distance, an averaging procedure over (random) *non-linear* transformations. For our goals, the choice of nonlinearity was motivated

by the following considerations: (1) a bounded non-linearity would be beneficial since unbounded non-linearities (such as cubic polynomials) have a pronounced deformation on the tails of a measure and may excessively weight outliers. (2) A sigmoid is another potential candidate, but it saturates at high values and we want the non-linearity to be similarly effective everywhere. (3) The use of polynomials has been discussed in [28], however, a full set of all higher order polynomials have exponential complexity and may be prohibitively expensive in high latent dimensions. We compared our method to cubic and quintic polynomials for the simple 3D spiral and found that the choice of the nonlinearity did not have a significant effect on performance, with our choice being the fastest (see Section F and Appendix E for computational time and loss comparisons). In principle, other ensembles of nonlinear transformations could be used.

B Pseudocode

Algorithm 1 Training EPSWAE

```

1: while not converged do
2:   Update the autoencoder  $\Psi_E, \Psi_D$ :
3:   for  $k_1$  substeps do
4:     Sample minibatch from data  $\{\mathbf{x}^{(1)}, \dots, \mathbf{x}^{(N)}\}$  with  $\mathbf{x}^{(j)} \sim P_X$ 
5:     Compute feature extractor samples  $\mathbf{f}^{(j)} = \Psi_{FE}(\mathbf{x}^{(j)})$ 
6:     Compute posterior samples  $\mathbf{z}^{(j)} = \Psi_E(\mathbf{x}^{(j)})$ 
7:     Compute decoded output  $\mathbf{x}_{recon}^{(j)} = \Psi_D(\mathbf{z}^{(j)})$ 
8:     Generate samples  $\{\xi^{(1)}, \dots, \xi^{(J)}\}$  with  $\xi^{(j)} \sim \mu$ 
9:     Compute prior samples  $\mathbf{y}^{(j)} = \Psi_{PE}(\xi^{(j)})$ 
10:    Compute reconstruction error:  $\mathcal{L}_{recon} = \frac{1}{J} \sum_{j=1}^J d(\mathbf{x}^{(j)}, \mathbf{x}_{recon}^{(j)})$ 
11:    Compute NSW distance:  $\mathcal{L}_{NSWdistance} = d_{NSW}(\frac{1}{N} \sum_{j=1}^N \delta_{\mathbf{z}^{(j)}}, \frac{1}{N} \sum_{j=1}^N \delta_{\mathbf{y}^{(j)}})$ 
12:    Compute FSC loss:  $\mathcal{L}_{FSC} = d_{FSC}(\{\mathbf{f}^{(1)}, \dots, \mathbf{f}^{(J)}\}, \{\mathbf{z}^{(1)}, \dots, \mathbf{z}^{(J)}\})$ 
13:    Compute autoencoder loss  $\mathcal{L}_{AE} = \alpha \mathcal{L}_{recon} + \beta \mathcal{L}_{NSWdistance} + \kappa \mathcal{L}_{FSC}$ 
14:    Compute gradients of  $\mathcal{L}_{AE}$  wrt to  $\phi_E, \phi_D$ 
15:    Update  $\phi_E, \phi_D$ 
16:  end for
17:  Update the prior-encoder  $\Psi_{PE}$ :
18:  for  $k_2$  substeps do
19:    Sample minibatch from data  $\{\mathbf{x}^{(1)}, \dots, \mathbf{x}^{(J)}\}$  with  $\mathbf{x}^{(j)} \sim P_X$ 
20:    Compute posterior samples  $\mathbf{z}^{(j)} = \Psi_E(\mathbf{x}^{(j)})$ 
21:    Generate samples  $\{\xi^{(1)}, \dots, \xi^{(J)}\}$  with  $\xi^{(j)} \sim \mu$ 
22:    Compute prior samples  $\mathbf{y}^{(j)} = \Psi_{PE}(\xi^{(j)})$ 
23:    Compute prior-encoder loss:  $\mathcal{L}_{PE} = d_{NSW}(\frac{1}{N} \sum_{j=1}^N \delta_{\mathbf{z}^{(j)}}, \frac{1}{N} \sum_{j=1}^N \delta_{\mathbf{y}^{(j)}})$ 
24:    Compute gradients of  $\mathcal{L}_{PE}$  wrt to  $\phi_{PE}$ 
25:    Update  $\phi_{PE}$ 
26:  end for
27: end while

```

C Architecture and Training Details

For all datasets, the prior-encoder Ψ_{PE} consists of three fully connected hidden layers and ReLU activations. For all datasets, the autoencoder and prior-encoder losses (given in Eqns 2 and 3) are trained iteratively using the optimizer Adam [1] with a learning rate of 0.001. We experimented with both $p = 1$ and $p = 2$ (corresponding to p-Wasserstein) in the SW distance and did not find any significant differences; all results in this paper use $p = 2$. For each calculation of the NSW distance, $L = 5$ random nonlinear transformations were taken followed by $M = 50$ one dimensional projections per transformation. Data-specific model and parameter details are given below.

3D Spiral dataset: The input to the prior-encoder is a 40D Gaussian, and the latent space is 3D. The input to the autoencoder is a 40D embedding of a 3D spiral manifold with 10% noise. The dataset consists of 10000 samples, and a batch size of 100 was used. The prior-encoder, the data encoder, and the decoder consist of three Fully Connected (FC) layers with 40 nodes each and ReLU activations. The reconstruction loss is given by the Mean Square Error and $\alpha = 1, \beta = 0.1, \kappa = 0.01$ in Eqn 2. In the absence of convolutional layers, the FSC term encourages the pairwise distances of the minibatch in latent space to be similar to the pairwise distances of the minibatch in the data space. The prior-encoder is trained $k_1 = 2$ times for each training of the autoencoder $k_1 = 1$. Power of distance $h = 2$ is used to compute edge weights for computing network-geodesics.

MNIST dataset: The input to the prior-encoder is a 40 dimensional *mixture of 10 Gaussians*, and the latent space is 5 dimensional. The data encoder takes MNIST images as input using a batch size of 100, and consists of the following layers Conv (1,10,3) \rightarrow BatchNorm \rightarrow ReLu \rightarrow MaxPool (2,2) \rightarrow Conv (10,16,3) \rightarrow BatchNorm \rightarrow ReLu followed by two FC layers of 512 and 256 nodes respectively with a leaky ReLu nonlinearity. The encoder outputs a 5 dimensional latent representation. The decoder consists of the reverse, i.e., three fully connected layers of size 256, 512, and 1936 nodes respectively. This is followed by ConvTranspose (16,10,3) \rightarrow LeakyReLu \rightarrow Upsample(2,2) \rightarrow ConvTranspose (10,1,3) \rightarrow Sigmoid. The decoder output has size 28×28 . The prior-encoder is trained $k_1 = 1$ times for each training of the autoencoder $k_2 = 1$. The reconstruction loss is given by the Binary Cross Entropy and $\alpha = 1, \beta = 0.1, \kappa = 0.001$ in Eqn. 2. The FSC loss encourages the pairwise distances of the minibatch in latent space to be similar to the pairwise distances of the minibatch in *feature* space computed at the output of the last convolutional layer in the data encoder. Energy parameter $h = 2$ is used to compute edge weights for computing network-geodesics.

CelebA dataset: The input to the prior-encoder is a 186 dimensional *mixture of 10 Gaussians*, and the latent space is 128 dimensional. We ran experiments with different latent dimensions and found that the generation ability didn't vary significantly as a function of latent dimension. We trade-off image quality of the input images for computational speed by downsizing the input and employ a fairly simple network compared to state of the art computer vision architectures that use CelebA. The data encoder takes CelebA images (of size $218 \times 178 \times 3$) and downsizes them to size $64 \times 64 \times 3$. The data encoder consists of the following layers Conv (3,16,3) \rightarrow BatchNorm \rightarrow ReLu \rightarrow MaxPool (2,2) \rightarrow Conv (16,32,3) \rightarrow BatchNorm \rightarrow ReLu \rightarrow MaxPool (2,2) \rightarrow Conv (32,64,3) \rightarrow BatchNorm \rightarrow ReLu followed by two FC layers of 512 and 256 nodes respectively with a leaky ReLu nonlinearity. The encoder outputs a 128 dimensional latent representation. As in the case of MNIST, the decoder consists of the reverse, with convolutions replaced by Convolution Transpose, and MaxPool replaced by Upsample. The output of the decoder is passed through a sigmoid nonlinearity and is of size $64 \times 64 \times 3$. The prior-encoder was trained

$k_1 = 1$ times for each training of the autoencoder. The reconstruction loss is given by the Binary Cross Entropy and $\alpha = 500, \beta = 50, \kappa = 0.05$ in Eqn. 2. The FSC loss encourages the pairwise distances of the minibatch in latent space to be similar to the pairwise distances of the minibatch in *feature* space, i.e., computed at the output of the last convolutional layer in the encoder. Energy parameter $h = 2$ is used to compute edge weights for computing network-geodesics.

D Spiral Baseline Comparisons

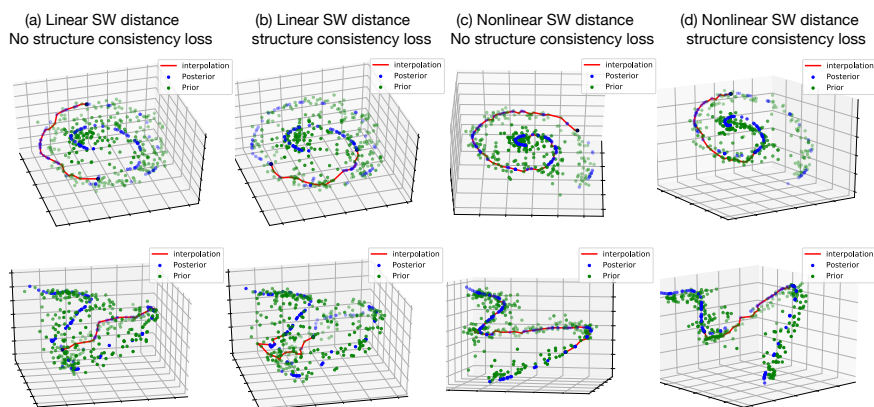


Fig. 6. Comparisons of the EPSWAE model with different loss terms. Top panels present top views, and bottom panels present the corresponding side views. The red curves show interpolation between two randomly selected samples using the network-geodesic algorithm. All figures are generated after 100 epochs with a lr=0.01, and batch size =100. $k_1 = 1, k_2 = 2$.

Figure 6 shows the effects of the different loss terms in EPSWAE on the geometry of the learned prior and posterior. The position and orientation of the spiral in the 3D plots are random and the views in the image are hand-chosen to be equivalent. (a) shows latent space and interpolations (red) using EPSWAE with a linear Sliced Wasserstein distance in the loss, and no structural consistency term. (b) shows that adding a structural consistency term doesn't remarkably improve the quality of the manifold learned, however, consistent with other experiments, it seems to improve interpolation slightly. Note here that since we don't use convolutional layers for the 3D spiral, the structural consistency term preserves distance in latent space corresponding to distances in data space. (c) shows that employing the NSW distance term significantly improves the learned structure in latent space. The improvements resulting from incorporation of the NSW and structural consistency terms as seen in these

visualizations of the 3D spiral lead us to use both loss terms (as in (d)) on all results in the main paper.

E Comparison with other Sliced Wasserstein nonlinearities

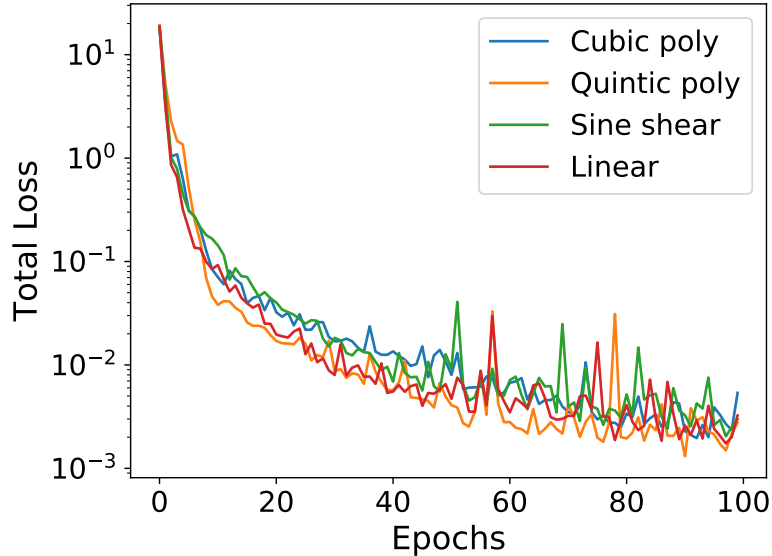


Fig. 7. Loss as a function of training epochs for linear SW, cubic nonlinearity, quintic nonlinearity and our (sine-shear) NSW distance. A full set of cubic and quintic functions terms are considered for computing the generalized Radon transform in the SW distance. $L = 5$ nonlinear transforms with $M = 50$ linear 1D projections each taken for all cases.

Here, we compare our choice of nonlinearity in the SW loss (sinusoidal shear) with some other common nonlinearities. While there exist several methods to improve the SW distance (e.g. max-SW [21] which has seen several subsequent variations), these involve additional training, and hence aren't considered (although many such versions of SW distance could be used in conjunction with our method). Instead we consider the polynomial generalized Radon transforms described in [28]. The computational cost of a single polynomial generalized Radon transform is $\mathcal{O}(d^k)$ for dimension d and k^{th} order of polynomial, and hence we limit our investigation to cubic and quintic polynomials. We show results on the artificial 3D Spiral dataset trained upto 100 epochs with $\alpha = 1$, $\beta = 0.1$,

$\kappa = 0.01$. We see in Fig. 7 that the choice of nonlinearity does not have a significant effect on the loss, however, as seen in Table F, the sine-shear has slightly lower computational cost.

F Computational cost of nonlinearities

The choice of nonlinearity was, in part, motivated by computational efficiency and simplicity, i.e., not requiring additional optimizations every evaluation or the training of a discriminator-like network to select optimal transformations. Our sinusoidal shear nonlinearity is closely related to a special case of the generalized SW distance defined in [28] (see discussion in Section 2.1 for differences). Here, we present a comparison of computational time with two polynomial-type nonlinearities discussed in [28] - cubic and quintic. Computations done on a laptop with Intel Core i7-10710 CPU, 16GB RAM, and computed over 1000 runs. In practice, the losses were indistinguishable with choice of nonlinearity (see Appendix E), whereas the sine shear is slightly less expensive (see Table 1 in Appendix F). However, the complexity of cubic and quintic nonlinearities are exponential in dimension and hence are impractical for larger data.

Table 1. Comparison of computational time for nonlinearities in SW distance.

	sine-shear NSW	cubic NSW	quintic NSW
Computational Cost	0.0050s \pm 0.0006s	0.0054s \pm 0.0007s	0.0060s \pm 0.0008s

G MNIST Generation Results

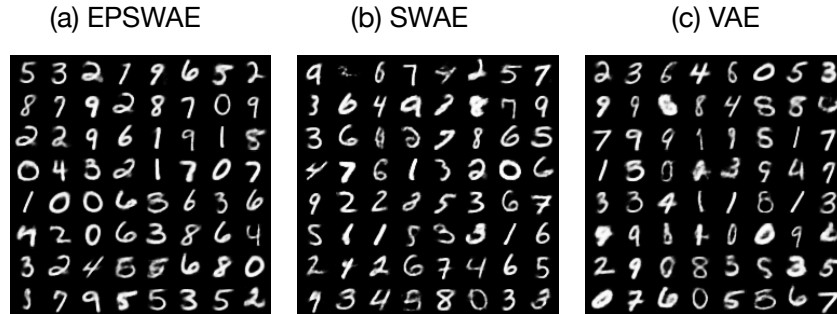


Fig. 8. Comparison between (a) EPSWAE (b) SWAE and (c) VAE for generation on MNIST. for all three, batch size = 200, epochs=100, lr = 0.001, for EPSWAE $k_1 = 2$, $k_1 = 1$, $\alpha = 1$, $\beta = 0.1$, $\kappa = 0.001$.

Figures 8 (a,b,c) shows generation on the MNIST dataset after 100 epochs on EPSWAE, baseline SWAE[20], and baseline VAE [1] respectively. All networks EPSWAE and baselines SWAE and VAE use equivalent architectures (outlined in Appendix C), and hyperparameters are optimized individually. As seen in the figure, we observe that EPSWAE generated samples were consistently found to have a lower fraction of ‘false’ digits, i.e., digits that are unrealistic.

H CelebA Generation Results

CelebA raw images are downsized to 64×64 pixels, and a simple architecture is employed (see Appendix C). This serves as a proof of principle for a better latent representation and interpolation, without a high computational cost. Naturally, using a more sophisticated network (for instance ResNet, VGG etc.) without downsizing the data would yield higher quality images at a computational cost.

Figure 9 shows generation on the CelebA dataset after 100 epochs with (a) EPSWAE and (b) baseline SWAE (right) respectively. Both employ equivalent architectures and take downsized images as input. As seen in the figure, EP-SWAE generated images are more realistic. Note that this comparison is for equivalent training epochs and architectural details, and does not make claims about the quality of SWAE images with longer training.



Fig. 9. Images generated from prior samples in (a) EPSWAE (b) Baseline SWAE. Batch size = 200, epochs=100, lr = 0.001. $\alpha = 500, \beta = 50, \kappa = 0.05$.

I Effect of energy parameter on CelebA interpolations

Additional CelebA interpolations are shown in Fig. 10. The length of interpolations is automatically selected by the network algorithm. In some cases, a linearly interpolated point is added between every two samples on the network-geodesic to make smoother transitions; this would be unnecessary with enough samples of the prior, however it could be impractical in high latent dimension to generated sufficiently many prior samples. Note that even if only one intermediate point is selected by the network geodesic, the generated interpolation could be significantly different from a purely linear interpolation (an illustration is provided in Figure 3.1 - the direct linear interpolation from A to B is significantly different from the interpolation through the point C). Fig. 10 presents a comparison between energy parameter $h = 1$ and $h = 2$. The energy parameter determines the power of the distance metric used to compute the edge weight. One can think of the higher value ($h = 2$) as corresponding to stronger connections between points, and encouraging shorter hops. In practice, as seen from the figure, there is no clear advantage to choosing a specific value of energy parameter h .



Fig. 10. Additional CelebA interpolations. The first and last images are reconstructions of real data, and the interpolations traverse through samples of the prior using the network-geodesic algorithm. (a) Top three panels show interpolations for energy parameter $h = 1$, and (b) bottom three panels show interpolations for energy parameter $h = 2$. Latent space is 128 dimensional. Hyperparameters are the same as those used in the paper. A total of a 400 samples in latent space are used.

J Linear interpolation comparison EPSWAE and SWAE

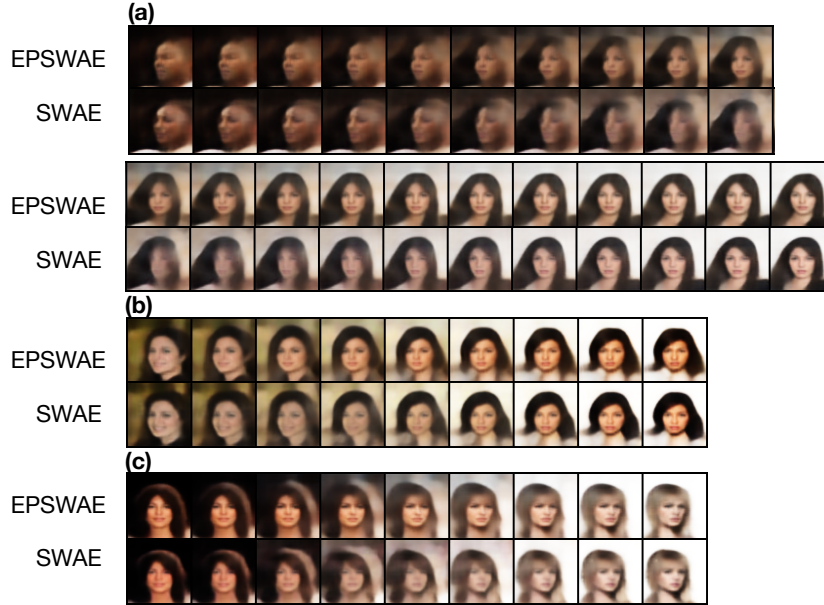


Fig. 11. Comparisons of linear interpolation between EPSWAE and SWAE. The first and last images are reconstructions of randomly picked real data (a) shows long interpolation (over two lines), (b,c) show shorter interpolations. Hyperparameters are the same as those used in the paper. Latent space is 128 dimensional. A total of a 400 samples in latent space are used.

We compare here linear interpolations on the CelebA dataset for MNIST and CelebA. The autoencoder networks used are identical and outlined in Section C. In contrast, EPSWAE uses the additional prior encoder. Both models are independently optimized, and the interpolations are linear. As seen in Fig. 11, interpolations in EPSWAE are more realistically identifiable as 'faces' than SWAE, which mixes up the features and generates blurry intermediate images. This is suggestive that the prior-encoder may play a role in improving latent representation.